



ASME Accepted Manuscript Repository

Institutional Repository Cover Sheet

Marcel

Matha

First

Last

ASME Paper Title: Advanced methods for assessing flow physics of the TU Darmstadt compressor stage:

Uncertainty quantification of RANS turbulence modeling

Authors: Marcel Matha, Felix M. Möller, Christoph Bode, Christian Morsbach, Edmund Kügeler

ASME Journal Title: Journal of Turbomachinery

Volume/Issue currently not known

Date of Publication (VOR* Online) 4 December 2024

<https://asmedigitalcollection.asme.org/turbomachinery/article/doi/10.1115/1.406731>

ASME Digital Collection URL: [nced-methods-for-assessing-flow-physics-of-the](https://asmedigitalcollection.asme.org/turbomachinery/article/doi/10.1115/1.406731)

DOI: <https://doi.org/10.1115/1.4067315>

*VOR (version of record)

Marcel Matha¹
 Institute of Propulsion Technology
 German Aerospace Center (DLR)
 Linder Höhe, 51174 Cologne, Germany
 email: marcel.matha@dlr.de

Felix M. Möller
 Institute of Test and Simulation for Gas
 Turbines
 German Aerospace Center (DLR)
 Linder Höhe, 51174 Cologne, Germany
 email: felix.moeller@dlr.de

Christoph Bode
 Institute of Jet Propulsion and Turbomachinery
 University of Braunschweig
 Hermann-Blenk-Straße 37, 38108
 Braunschweig, Germany
 email: chr.bode@tu-braunschweig.de

Christian Morsbach
 Institute of Propulsion Technology
 German Aerospace Center (DLR)
 Linder Höhe, 51174 Cologne, Germany
 email: christian.morsbach@dlr.de

Edmund Kügeler
 Institute of Propulsion Technology
 German Aerospace Center (DLR)
 Linder Höhe, 51174 Cologne, Germany
 email: edmund.kuegeler@dlr.de

Advanced methods for assessing flow physics of the TU Darmstadt compressor stage: Uncertainty quantification of RANS turbulence modeling

In this paper, we quantify the turbulence modeling uncertainty for the transonic TUDa compressor. The present work applies the Eigenspace Perturbation Framework (EPF), as it is the only published physics-based framework capable of addressing the model-form uncertainty in turbulence closure modeling. To sample from the possible solution space and obtain the modeling uncertainty, we perform simulations perturbing the eigenvalues of the Reynolds stress tensor in addition to simulations using an unperturbed turbulence model. We show that the shape of the Reynolds stress tensor ellipsoid has significant impact on the evolution of turbulence, flow separation, vortex systems, shock-boundary layer interaction and finally the overall performance of the compressor. We compare the estimated uncertainties with available measurements and transitional Delayed Detached-Eddy Simulations (DDES). This allows us to assess the confidence of the chosen turbulence model and to evaluate the sharpness and coverage of the resulting uncertainty bounds. Thus, the EPF is comprehensively validated and suggestions for its future applicability with respect to turbomachinery components are made.

Keywords: CFD, RANS, turbulence modeling, uncertainty quantification, compressor stage

1	Nomenclature		
2	Roman letters		
3	a_{ij} = Reynolds stress anisotropy tensor [-]		
4	k = Turbulent kinetic energy [$\text{m}^2 \text{s}^{-2}$]		
5	L_T = Turbulent length scale [m]		
6	\dot{m} = Mass flow rate [kg s^{-1}]		
7	Ma = Mach number [-]		
8	Ma_{is} = Isentropic Mach number [-]		
9	n = Rotational speed [rpm]		
10	p = Pressure [Pa]		
11	P_k = Turbulence production term [$\text{m}^2 \text{s}^{-3}$]		
12	S_{ij} = Strain rate tensor [s^{-1}]		
13	T = Temperature [K]		
14	u_i = Velocity vector [m s^{-1}]		
15	v_i = i th eigenvector of anisotropy tensor [-]		
16	v_{ij} = Eigenvalue matrix of anisotropy tensor [-]		
17	\mathbf{x} = Barycentric coordinate vector [-]		
18	x_i = Cartesian coordinate [m]		
19	Greek letters		
20	γ = Heat capacity ratio [-]		
21	δ_{ij} = Kronecker delta [-]		
22	Δ_B = Relative perturbation magnitude [-]		
23	ϵ_{ijk} = Levi-Civita symbol [-]		
24	ζ_t = Total temperature ratio [-]		
25	η_{is} = Isentropic efficiency [-]		
26	λ_i = i th eigenvalue of anisotropy tensor[-]		
27	Λ_{ij} = Eigenvalue matrix of anisotropy tensor[-]		
28	ν_T = Turbulent eddy viscosity [$\text{m}^2 \text{s}^{-1}$]		
		Π_t = Total pressure ratio [-]	29
		τ_{ij} = Reynolds stress tensor [$\text{m}^2 \text{s}^{-2}$]	30
		ω = Specific turbulent dissipation rate [s^{-1}]	31
		ω_{sw} = Streamwise vorticity [s^{-1}]	32
		Superscripts and subscripts	33
		* = Perturbed quantity	34
		1C = One-component turbulence	35
		2C = Two-component turbulence	36
		3C = Three-component turbulence	37
		15 = Quantity at ME15	38
		21 = Quantity at ME21	39
		30 = Quantity at ME30	40
		corr = Corrected quantity	41
		exp = Experimentally determined value	42
		\mathbf{i} (j,k,q) = Vector quantity	43
		\mathbf{ij} (in, nl, jl) = Matrix quantity	44
		ISA = Quantity at International Standard Atmosphere	45
		real = Real quantity	46
		stall = Quantity at compressor stall	47
		(t) = Target	48
		t = Total (stagnation) quantity	49
		1 Introduction	50
		The design of turbomachinery components is heavily dependent on the prediction capabilities of Reynolds-averaged Navier-Stokes (RANS) simulations. However, the RANS equations require the modeling of the second-moment Reynolds stress tensor τ . While Reynolds stress tensor modeling, known as turbulence modeling, provides practicality and enables efficient simulations, it also comes with inherent limitations that hinder the attainment of high	51
			52
			53
			54
			55
			56
			57

¹Corresponding Author.
 November 27, 2024

58 levels of accuracy. Over the last decade, researchers have high-
59 lighted the limitations of the commonly applied Linear Eddy Vis-
60 cosity Model (LEVM) assumption for flow situations not covered
61 by the calibration cases [1–4]. Due to the lack of knowledge, these
62 LEVMs are characterized by modeling assumptions derived from
63 data observation, engineering intuition and computational pragmat-
64 ism, leading to a significant degree of model-form (epistemic) un-
65 certainty. This is in contrast to potential errors in Computational
66 Fluid Dynamics (CFD) that are not due to the general lack of
67 knowledge, such as discretization or round-off errors, which could
68 in principle be reduced by exploiting extra resources [5]. Theo-
69 retically, epistemic uncertainties could also be mitigated through a
70 better understanding of turbulent processes, facilitating the devel-
71 opment of advanced models. This contrasts with aleatory uncer-
72 tainties, such as manufacturing tolerances or uncertain operating
73 conditions, which cannot be reduced and are not within the scope
74 of the present study. In the past, efforts in engineering design
75 applications aimed to address uncertainties in CFD simulations
76 through the use of safety margins, levels of redundancy and sim-
77 ilar heuristic approaches. As computational resources continue to
78 increase, the turbomachinery industry is undergoing substantial ad-
79 vancements in digitization. Methodologies such as robust design
80 or reliability-based design offer the potential to supersede the tra-
81 ditional approaches for addressing uncertainties in CFD. In recent
82 years, there has been a growing interest in Uncertainty Quantifi-
83 cation (UQ), paving the way for more reliable simulation-based
84 designs [6].

85 The usage of turbulence closure models represents a major
86 source of the overall uncertainty observed in RANS simulations,
87 assuming a known set of boundary conditions and precise geome-
88 try information. In addition, the quantification of model-form un-
89 certainty is described to be the ‘greatest challenge’ in CFD [7].
90 Following Duraisamy’s categorization, the uncertainty is intro-
91 duced at several modeling levels [8]. These include uncertain-
92 ties arising from information loss during the averaging of the
93 Navier-Stokes equations, uncertainties associated with representing
94 Reynolds stress as a function of mean flow quantities, uncertain-
95 ties stemming from the selection of a particular function (mainly
96 transport equations) and uncertainties associated with choosing and
97 calibrating certain parameters. Two broad categories are recog-
98 nized: parametric and non-parametric approaches. Parametric un-
99 certainties originate from the selection and calibration of closure
100 coefficients, whereas non-parametric methodologies explore uncer-
101 tainties related to the mathematical relationships for representing
102 the Reynolds stress tensor [9]. As the modeled Reynolds stress
103 tensor is the only term that links the turbulence model equations
104 to the RANS equation, it plays a unique role. Hence, our current
105 research focuses on the appropriate estimation of turbulence model-
106 ing uncertainty related to the functional representation of Reynolds
107 stresses (non-parametric approach). In this paper, we introduce se-
108 lective perturbed states of the Reynolds stress tensor based on the
109 concept of realizability. This physics-based approach developed
110 by Emory et al. [10] is able to address the epistemic uncertainty
111 inherent in turbulence closure modeling. As the modifications to
112 the Reynolds stress tensor rely on perturbing its eigenspace (de-
113 scribed in Section 2), the entire framework is called the Eigenspace
114 Perturbation Framework (EPF).

115 Due to its unique characteristics and persuasive interpretabil-
116 ity of its simulation outcomes, the EPF has been used in vari-
117 ous engineering applications, such as aircraft design [11], civil
118 structural design [12], wind farms [13,14] and turbomachinery
119 flows [15]. For this reason, the EPF has also been integrated into
120 TRACE [16,17], which is developed by the German Aerospace
121 Center (DLR) in strong cooperation with MTU Aero Engines AG.
122 We have already verified the conceptual idea behind the methodol-
123 ogy and its computational implementation and applied the EPF
124 to generic test cases in recent publications [18,19]. Although
125 the aforementioned applications of the EPF have provided some
126 validation of the framework, this paper applies and consequently
127 validates the methodology to the most complex configuration re-

lated to turbomachinery applications to date. The capabilities of
the EPF are demonstrated on the Technische Universität Darmstadt
(TUDa) compressor [20]. The TUDa-GLR-OpenStage compressor
is a single-stage, transonic axial compressor, which is introduced
in Section 3.

Hence, the novelty of this paper lies in the application of the
Reynolds stress tensor perturbation to a complex rotational multi-
row test case on the one hand. With respect to physical flow
phenomena, this means shock-boundary layer interaction in the ro-
tor section, formation of a rotor tip vortex and general rotor-stator
interaction. On the other hand, the current research offers the
physically constrained estimation of the turbulence modeling un-
certainty for RANS simulations of this test case. Hereby this paper
contributes to the ongoing assessment of the overall uncertainties
of simulating the TUDa compressor [21–23].

2 Eigenspace perturbation method

State-of-the-art LEVMs close the RANS equations by introduc-
ing a scalar turbulent eddy viscosity ν_T to express the Reynolds
stress tensor

$$\tau_{ij} = -2\nu_T \left(S_{ij} - \frac{1}{3} \frac{\partial u_k}{\partial x_k} \delta_{ij} \right) + \frac{2}{3} k \delta_{ij}, \quad (1)$$

where $k = \frac{1}{2} \tau_{ii}$ represents the turbulent kinetic energy and the
strain-rate tensor is denoted as S_{ij} . This modeling assumption,
known as the Boussinesq assumption, assumes turbulence to be-
have as an isotropic medium. Hence, LEVMs are not able to
account correctly for the anisotropy of Reynolds stresses by defini-
tion, leading to a significant degree of epistemic uncertainty. Fol-
lowing the modeling assumption in Eq. (1), the eigenspace of the
Reynolds stress tensor only depends on the eigenspace of the strain-
rate tensor (identical eigenvectors and linear dependency between
eigenvalues). The EPF, described in the following, assesses this
uncertainty within physical constraints. The underlying methodol-
ogy is based on the spectral decomposition of the anisotropic
part, represented by the anisotropy tensor \mathbf{a} , of the Reynolds stress
tensor

$$\tau_{ij} = k \left(a_{ij} + \frac{2}{3} \delta_{ij} \right) = k \left(v_{in} \Lambda_{nl} v_{jl} + \frac{2}{3} \delta_{ij} \right). \quad (2)$$

The eigenvectors \mathbf{v}_k of a_{ij} are contained column-wise in v_{in} , while
the traceless diagonal matrix Λ_{nl} contains the corresponding eigen-
values λ_k .

Generally speaking, perturbing the Reynolds stress tensor means
changing the amount of turbulent kinetic energy (k), the spectral
energy distribution of the anisotropy tensor (λ_k) and the orientation
of the principal components of the anisotropy tensor (v_{in}) [24,25].
The eigenspace perturbation, considered in this study, modifies
solely the shape of the Reynolds stress tensor ellipsoid by creating
perturbed states of the eigenvalues λ_k^* , while the other two at-
tributes of the Reynolds stress tensor are kept constant. Changing
the shape of the Reynolds stress tensor ellipsoid means modifying
the turbulence model to an orthotropic eddy viscosity model, where
turbulence behaves differently along each eigendirection [26]. This
is equivalent to assigning different turbulent eddy viscosities along
every eigendirection. Consequently, the uniform linear dependency
between the eigenvalues of the strain-rate tensor and the Reynolds
stress tensor is overridden. Accordingly, the perturbed Reynolds
stress tensor is defined as

$$\tau_{ij}^* = k \left(v_{in} \Lambda_{nl}^* v_{jl} + \frac{2}{3} \delta_{ij} \right). \quad (3)$$

The realizability constraints manifest limits for the eigenvalues
of the Reynolds stress tensor and the anisotropy tensor, respec-

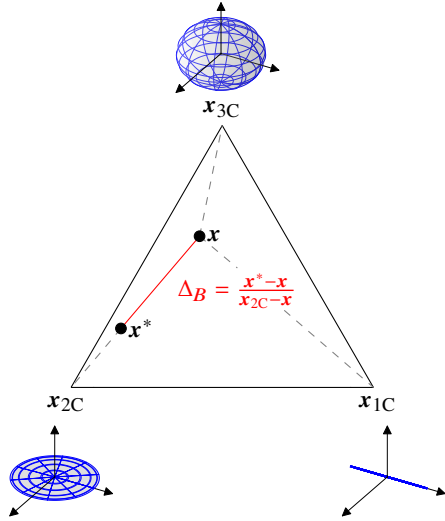


Fig. 1 Systematic representation of the Reynolds stress tensor's eigenvalue perturbation within the barycentric triangle. Its effect on the shape of the Reynolds stress tensor is shown by the gray ellipsoid visualizations, when approaching the vertices of the triangle.

tively [27]. The mapping of eigenvalues onto barycentric coordinates, based on Banerjee et al. [28],

$$\mathbf{x} = \frac{1}{2} \mathbf{x}_{1C} (\lambda_1 - \lambda_2) + \mathbf{x}_{2C} (\lambda_2 - \lambda_3) + \mathbf{x}_{3C} \left(\frac{3}{2} \lambda_3 + 1 \right) \quad (4)$$

is used to explore the realizable eigenvalue space within a 2D projection, where $\mathbf{x}_{1C}, \mathbf{x}_{2C}, \mathbf{x}_{3C}$ are the coordinates of the vertices of an equilateral triangle, as illustrated in Fig. 1. The states of the Reynolds stress tensor that are defined by these vertices represent the limiting states of turbulence componentiality based on the number of non-zero eigenvalues of the Reynolds stress tensor: the three-component, isotropic limit (3C), the two-component axisymmetric limit (2C) and the one-component limit (1C). As the representation of eigenvalues in barycentric coordinates enables linear interpolation between two states, Emory et al. [24] propose to obtain the perturbed location as a relative shift towards the vertices $\mathbf{x}_{(t)} \in \{\mathbf{x}_{1C}, \mathbf{x}_{2C}, \mathbf{x}_{3C}\}$ according to

$$\mathbf{x}^* = \mathbf{x} + \Delta_B (\mathbf{x}_{(t)} - \mathbf{x}) \quad \text{with } \Delta_B \in [0, 1]. \quad (5)$$

This is shown by way of example in Fig. 1 for the perturbation towards the 2C state. As Eq. (4) can be expressed as $\mathbf{x} = \mathbf{Q}\boldsymbol{\lambda}$, the resulting perturbed eigenvalues are determined via

$$\boldsymbol{\lambda}^* = (1 - \Delta_B) \boldsymbol{\lambda} + \Delta_B \boldsymbol{\lambda}_{(t)}, \quad \text{while} \quad (6)$$

$\boldsymbol{\lambda}_{(t)} \in \{\boldsymbol{\lambda}_{1C}, \boldsymbol{\lambda}_{2C}, \boldsymbol{\lambda}_{3C}\} = \left\{ \left(\frac{4}{3}, -\frac{2}{3}, -\frac{2}{3} \right)^T, \left(\frac{1}{3}, \frac{1}{3}, -\frac{2}{3} \right)^T, (0, 0, 0)^T \right\}$ depends on the chosen componentiality of the target state [26]. While the choice of $\Delta_B = 0$ results in unaltered eigenvalues, $\Delta_B = 1$ changes the eigenvalues to the ones of the target state $\boldsymbol{\lambda}_{(t)}$. Whereas previous studies tried to account for spatially varying perturbations [10,17,29,30], we assume a uniform distribution of the relative perturbation magnitude Δ_B in the computational domain. Although LEVMs produce sufficiently accurate predictions in the majority of the computational domain, except for separation, reattachment, secondary flows and wakes, we are exploring the worst case scenario by applying uniform, non-local perturbations. This procedure results in the most conservative uncertainty estimates.

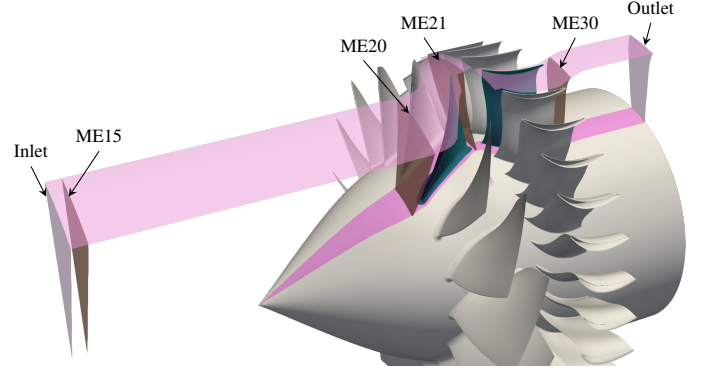


Fig. 2 3D illustration of the considered TUDa compressor configuration. The simulated single passage is colored in pink, while reference locations are highlighted as well.

The eigenspace perturbation takes place in every grid point within each pseudo-time step of the steady simulations. The coupling with the RANS equations is done by updating the viscous fluxes via the perturbed Reynolds stress tensor. To incorporate the effect on the turbulence model's turbulent kinetic energy transport equation, the production of turbulent kinetic energy is computed according to

$$P_k = -\tau_{ij}^* \frac{\partial U_i}{\partial x_j}, \quad (7)$$

incorporating the perturbed Reynolds stresses explicitly. Finally, the uncertainty on certain Quantities of Interest (QoI) attributed to the uncertainty of the turbulence model can be determined by propagating the perturbed Reynolds stress tensors in additional RANS simulations and sample from the attainable possible solution space.

3 TUDa-GLR-OpenStage compressor

3.1 Test case description. The single stage transonic axial compressor is an open test case of the Global Power and Propulsion Society (GPPS) providing detailed information on the geometry and a comprehensive set of measurement data by the Technical University of Darmstadt [20]. The original stage consists of 16 rotor blades, 29 stator blades and 5 outlet guide vanes. At the International Standard Atmosphere (ISA) corrected design speed of $n_{\text{corr}} = n_{\text{real}} \sqrt{\frac{T_{\text{ISA}}}{T_{i,15}}} = 20\,000$ rpm and a corrected mass flow rate of $\dot{m}_{\text{corr}} = \dot{m}_{\text{real}} \frac{p_{\text{ISA}}}{p_{i,15}} \sqrt{\frac{T_{i,15}}{T_{\text{ISA}}}} = 16.00$ kg/s, a total pressure ratio of 1.5 is achieved.

3.2 CFD setup. TRACE is a parallel Navier-Stokes flow solver. In the present work we use the finite-volume method to discretize the compressible RANS equations. We apply Roe's upwind scheme combined with MUSCL extrapolation to ensure second-order accuracy. Large gradients are smoothed using a van Albada-type flux limiter. This ensures the total variation diminishing property of the scheme, which is important for transonic flows. The attainment of steady-state solutions is facilitated through the utilization of an implicit time-marching algorithm. Furthermore, for the transport equations governing turbulence quantities, we apply a segregated solution method that is second-order accurate and conservative [31]. The two-equation, Menter SST $k - \omega$ [32] LEVM is chosen to be the underlying turbulence model in the present investigation. As already described in Section 2, the viscous fluxes and the turbulence production term are modified when applying the EPF.

We simulate a single passage of the compressor without considering the outlet guide vanes (see Fig. 2). Previous studies already presented a comprehensive analysis of various important aspects

Table 1 Number of grid points / 10^6 used for the RANS grid convergence study presented in Fig. 3.

	Total	Rotor	Stator
Ultra-coarse	0.70	0.30	0.29
Coarse	1.87	0.78	0.80
Medium	3.97	1.64	1.69
Fine	5.38	2.21	2.30
Ultra-fine	18.06	7.35	7.76

when simulating the compressor stage [21,22]. Based on recent adjustments of the geometry provided by the GPPS, our numerical setup incorporates the latest hub and shroud contour, the rotor tip gap of 0.75mm, a constant fillet radius at the rotor hub of 5mm and approximated fillet radii at stator hub and tip. We stick to using 16 rotor blades but scale to 32 stator blades in order to compare the RANS uncertainty estimates with the transitional Delayed Detached-Eddy Simulations (DDES) data of Möller et al. [33]. By comparing CFD with CFD results, we are able to eliminate potential geometrical errors. The inlet section of the computational domain is located 3% upstream of ME15 with respect to the compressor core axial length (ME20 to ME30). Experimentally measured total temperature and pressure profiles based on the experiment by Klausmann et al. [20] are prescribed at the inlet. Similar to previously published RANS studies (e.g. by He et al. [21]), we assume axial inflow direction, while the level of turbulence intensity is set to 4% and the turbulent length scale is assumed to be $L_T = \sqrt{k}/\omega = 0.09$ mm. The rotor-stator interface is accomplished by a mixing plane approach [34]. The domain's outlet is located at +58% downstream of ME30 with respect to the compressor core axial dimension. In order to compare RANS results at the experimental operating points, the respective mass flow rates are realized by using a boundary controller that adjusts the static pressure at the outlet of the computational domain. If the simulation, enforcing a certain mass flow rate, does not converge, an iterative process decreasing the backpressure in steps of 100 Pa is conducted. Hereby, we are able to examine the numerical stall limit of the RANS simulations appropriately.

Finally, given the geometry information by GPPS, the low-Reynolds mesh is generated using our in-house tool PyMesh. A grid convergence study based on 5 grids helps to identify the influence of grid resolution on the prediction of design relevant integral quantities. The considered grids are summarize in Table 1. As the goal of the conducted grid study is only to select a resolution that serves practical purposes for subsequent UQ simulations while still remaining computationally feasible, all simulations are based on the mass flow controller aiming for the experimental mass flow rates. Figure 3 shows the sensitivity with respect to the chosen grid resolution on the total pressure ratio

$$\Pi_{t,30-15} = \frac{P_{t,30}}{P_{t,15}} \quad (8)$$

and on the isentropic efficiency

$$\eta_{is} = \frac{\Pi_{t,30-15}^{((\gamma-1)/\gamma)} - 1}{\zeta_{t,30-15} - 1}, \quad (9)$$

where the total temperature ratio is defined as

$$\zeta_{t,30-15} = \frac{T_{t,30}}{T_{t,15}}. \quad (10)$$

These integral quantities are computed using the area-averaged total pressure and total temperature at ME30 and ME15.

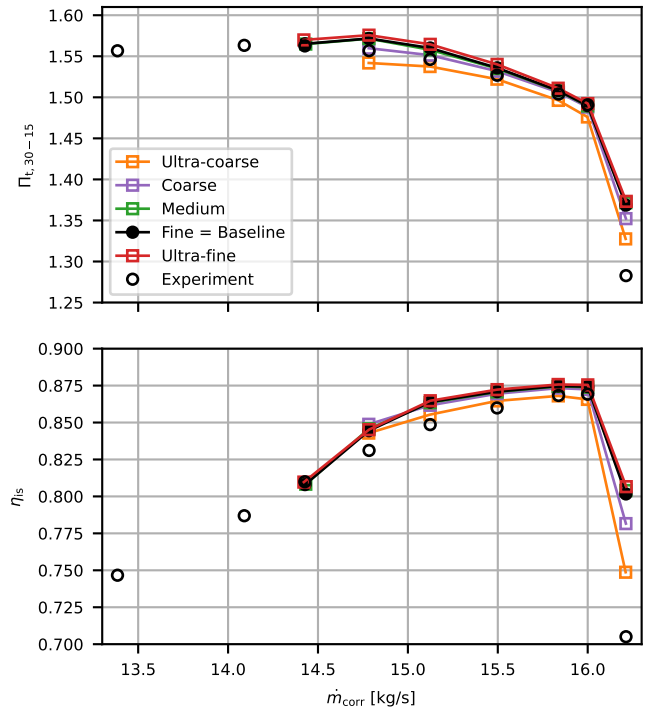


Fig. 3 Effect of grid resolution on the prediction of total pressure ratio (top) and isentropic efficiency (bottom) by RANS at 100% speedline.

The general trend indicates that mesh refinement results in an increase in both total pressure ratio and isentropic efficiency. Simultaneously, this is reflected in the ability to approach the experimentally determined stall limit. It also becomes evident that coarser meshes increase the matching with absolute values of total pressure ratio and isentropic efficiency ascertained in the experiment by Klausmann et al. [20]. This is in accordance with the observed grid analysis by He et al. [21]. Nevertheless, as we want to choose an appropriate level of grid convergence, we choose the fine mesh for the subsequent analysis and call the obtained results to be the baseline simulation in the following sections. Choosing the fine mesh leads to a 0.17% deviation in predicting the total pressure ratio and 0.13% difference in predicting the isentropic efficiency compared with the ultra-fine mesh at the design (peak efficiency) operation point. When we compare the prediction of the fine with the ultra-fine mesh resolution across all considered mass flow rates, the mean relative deviation for $\Pi_{t,30-15}$ is 0.26% and for η_t is 0.2%.

3.3 Creating uncertainty estimates based on Reynolds stress tensor perturbation. We perform simulations propagating Reynolds stresses that are perturbed towards the one-component (1C), two-component (2C) and isotropic limit of turbulence (3C). Following the approach proposed in our previous work [18,19], the relative perturbation magnitude with respect to the relative shift in barycentric coordinates Δ_B (see Fig. 1) is adjusted as a consequence of occurring convergence issues. Selecting a uniform Δ_B for 1C, 2C and 3C perturbation would be a conceivable and equally valid approach. Furthermore, it is also possible to moderate the Δ_B based on expert knowledge, marker functions [10] or machine learning [17,30]. In the present investigation, we apply Δ_B as large as possible non-uniformly towards x_{1C}, x_{2C}, x_{3C} in order to obtain the worst case scenario with respect to the inherent turbulence modeling uncertainty and to account for physically plausible variation in perturbation magnitude across the turbulence limiting states. As already described in Section 3.2, we aim for approaching the exper-

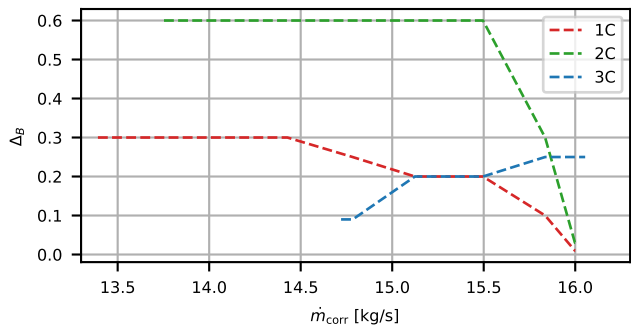


Fig. 4 Attainable relative perturbation magnitude Δ_B over corrected mass flow rate for eigenvalue perturbation of the Reynolds stress tensor towards the three limiting states of turbulence.

342 imental operating points (in terms of mass flow rates) at the design
 343 rotational speed. As previous studies (e.g. [35,36]) reveal, there is
 344 a general trend indicating more conservative uncertainty estimates
 345 when increasing the eigenvalue perturbation strength, we seek for
 346 the largest possible Δ_B for each individual operation point. Con-
 347 sidering that, we limited the iterative search to gradually decreasing
 348 Δ_B by 0.1 for $\Delta_B \in [0.1, 1.0]$ and by 0.01 for $\Delta_B \in [0, 0.1]$. Ad-
 349 ditionally, we employ an initially arbitrarily chosen search points
 350 at $\Delta_B = 0.25$. As soon as we switch the boundary condition at the
 351 outlet from mass flow controller to constant backpressure for ap-
 352 proaching the stall limit (described in Section 3.2) and some near
 353 choke operation point beyond the design point, we keep the rela-
 354 tive perturbation magnitude constant and evaluate the attainable
 355 backpressure adjustment.

356 4 Turbulence model uncertainty for a multi-row 357 compressor application

358 **4.1 Perturbation magnitude and effect on anisotropy.** Fol-
 359 lowing the procedure described in Section 3.3, Fig. 4 shows the
 360 attainable perturbation magnitude for each speedline simulation of
 361 1C, 2C and 3C. Throttling the compressor enables increased per-
 362 turbation magnitude for 1C and 2C perturbations, while Δ_B needs
 363 to be reduced for 3C simulations. To give an idea of what pertur-
 364 bing the eigenvalues means for the converged states of the Reynolds
 365 stress tensor, Fig. 5 presents the analysis of the Reynolds stress
 366 anisotropy at ME30 with respect to RGB coloring in Fig. 5(a) and
 367 the barycentric coordinates in Fig. 5(b). Evaluating the anisotropy
 368 tensor for the unperturbed baseline simulation using the Menter
 369 SST $k - \omega$ LEVM reveals the Reynolds stress tensor to be rather
 370 isotropic aligning the barycentric coordinates around the plane-
 371 strain line [28]. Except for the wakes and the secondary flow
 372 structures (see later analysis on secondary flows referring to Fig. 10
 373 and Fig. 11), where some areas tend towards the two-component
 374 corner of the barycentric triangle (green regions in Fig. 5(a)). At
 375 the chosen mass flow rate $\dot{m}_{corr} = 14.78$ kg/s, Δ_B is 0.25, 0.6
 376 and 0.09 for 1C, 2C and 3C perturbation respectively (cf. Fig. 4).
 377 This results in the expected shift of the barycentric coordinates
 378 in the direction of the respective vertex. The perturbation of the
 379 eigenvalues of the Reynolds stress tensor has to be done iteratively,
 380 allowing the mean flow quantities to change over simulation time
 381 until converged states are reached. The same holds true for the
 382 unperturbed state of the Reynolds stress tensor derived from the
 383 respective velocity gradients, turbulent kinetic energy and turbulent
 384 eddy viscosity (see Boussinesq assumption in Eq. (1)). Since the
 385 perturbation of the eigenvalues depends on the unperturbed state
 386 of the current iteration step, each converged perturbed data point
 387 in Fig. 5(b) is not simply shifted towards the corners by the relative
 388 perturbation magnitude starting from the baseline computation.

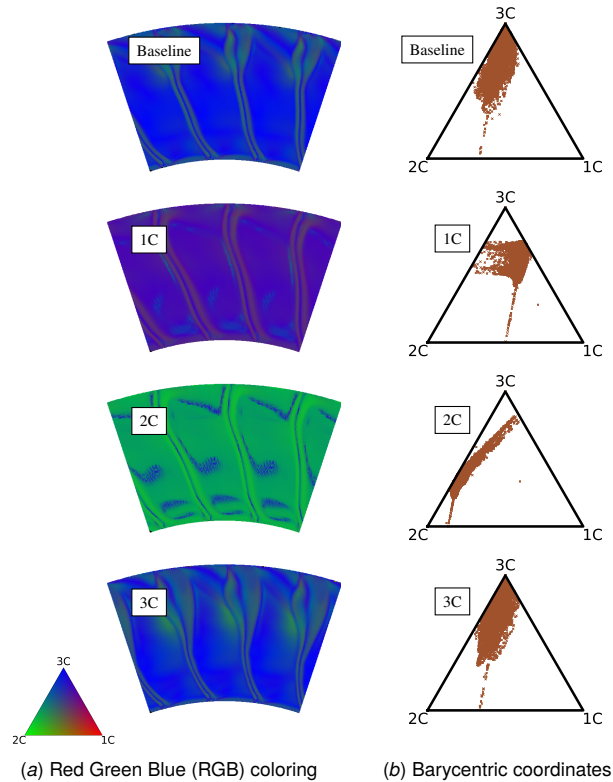


Fig. 5 Illustration of the turbulent state of the Reynolds stress tensor at ME30 and $\dot{m}_{corr} = 14.78$ kg/s. (a) presents the RGB coloring according to the location of each data point inside the barycentric triangle, which is shown in (b).

389 **4.2 Overall compressor performance.** Changing the eigen-
 390 values of the Reynolds stress tensor towards the one- and two-
 391 component limiting state of turbulence, stabilizes the RANS for
 392 low mass flow rates, as can be seen in Fig. 6. This leads to the
 393 possibility of further throttling the compressor compared with the
 394 baseline and 3C simulation. Unfortunately, we were not able to
 395 achieve converged steady-state RANS solutions significantly above
 396 the design mass flow rate, when perturbing the Reynolds stress
 397 tensor. On the one hand, this was already looming for 1C and 2C
 398 simulations, as we had to reduce Δ_B when approaching the design
 399 point to achieve converged solutions. On the other hand, 3C per-
 400 turbation beyond the design point lead to undesired instabilities,
 401 which may potentially be identified as choking. The predictions
 402 of the compressor performance based on the 3C simulations show
 403 reduced total pressure ratios and isentropic efficiencies over the
 404 entire speedline. Overall, the chosen perturbation magnitude seems
 405 to be too large for 3C. However, as mentioned in Section 3.3, we
 406 are aiming for worst case scenarios of the attainable turbulent states
 407 rather than accurate sharpness (appropriate bounding of CFD pre-
 408 dictions) of the uncertainty estimation. Consequently, we continue
 409 to analyze the obtained results based on the isotropic perturba-
 410 tions throughout this paper. Generally, the estimated uncertainty
 411 intervals for the integral compressor performance parameters in-
 412 clude most of the experimental measurements, constituting a good
 413 coverage of the considered EPF. Applying the unperturbed (base-
 414 line) turbulence model yields mostly increased efficiency and total
 415 pressure ratios compared with the considered perturbed ones.
 416 However, close to the numerical stall limit the baseline simula-
 417 tion reveals a rather abrupt reduction in compressor performance,
 418 whereas perturbing the Reynolds stress tensor towards the one- and
 419 two-component turbulence allows stable operations of the com-
 420 pressor with increased efficiency. Increased performance of the
 421 compressor enables a shift of the numerical stall limit to reduced

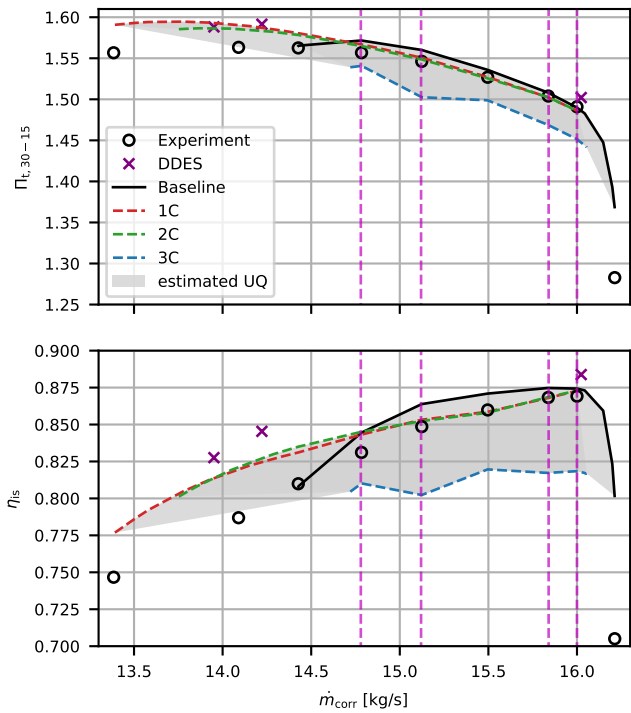


Fig. 6 Estimated turbulence modeling uncertainty for the global compressor performance quantities total pressure ratio (top) and isentropic efficiency (bottom) at 100% speedline and comparison with experimental data. The mass flow rates for subsequent detailed analysis are highlighted by magenta dashed lines ($\dot{m}_{corr} \in [14.78 \text{ kg/s}, 15.12 \text{ kg/s}, 15.84 \text{ kg/s}, 16.00 \text{ kg/s}]$).

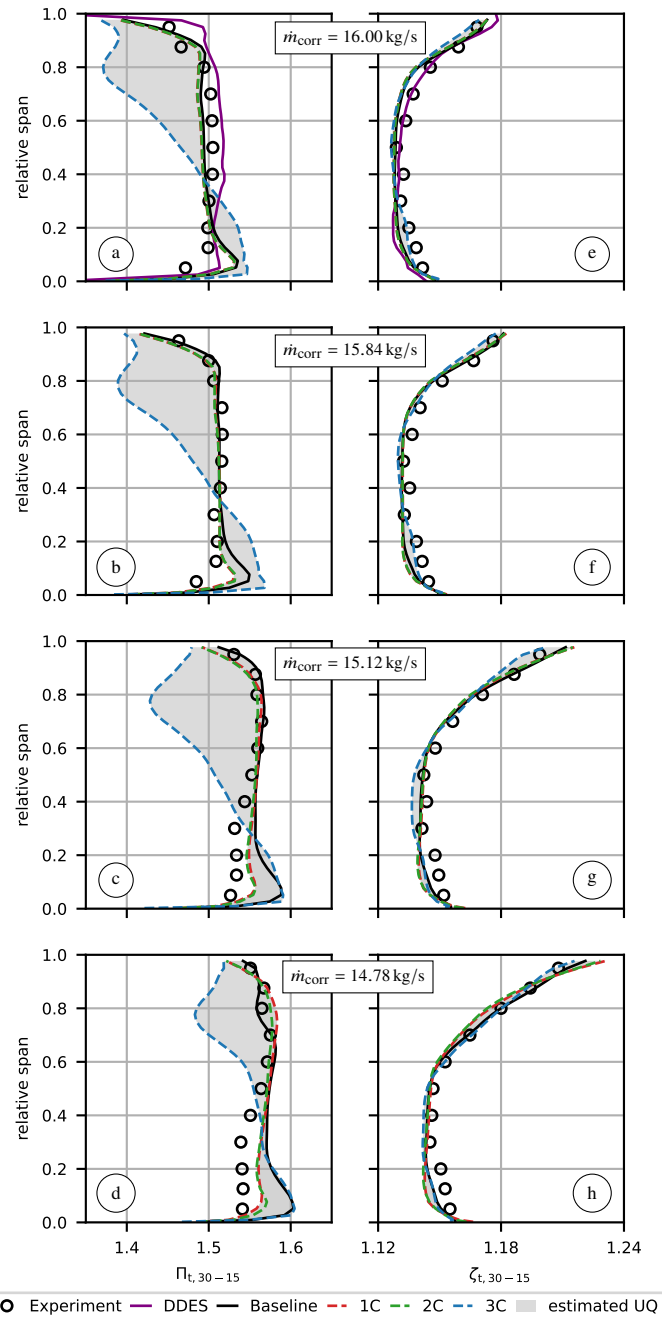


Fig. 7 Uncertainty estimates for predicting radial profiles of total pressure ratio ((a), (b), (c), (d)) and total temperature ratio ((e), (f), (g), (h)) at ME30 for four different operating points. The total pressure and temperature ratio is computed using circumferentially area-averaged quantities at ME30 and the integral area-averaged quantities at ME15.

422 mass flows by $\dot{m}_{corr1C, stall} - \dot{m}_{corr3C, stall} \approx -1.33 \text{ kg/s}$. Thus, perturbing
 423 towards 1C is beneficial for the prediction of the compressor's
 424 stall limit, as the difference between experimental and numerical
 425 stall mass flow rate becomes $\dot{m}_{corr_{exp, stall}} - \dot{m}_{corr1C, stall} \approx -0.01 \text{ kg/s}$.
 426 The performance maps in Fig. 6 also show the considered operation
 427 points by Möller et al. [33] using transitional DDES modeling. Be-
 428 sides the increased number of grid points, the applied geometrical
 429 model of the compressor is identical to the one used in the present
 430 RANS study. However, the transitional DDES are combined with
 431 the stagnation point anomaly fix by Kato and Launder [37] and
 432 the rotational effects extension by Bardina et al. [38], which is per
 433 se a numerical setup deviating from the one used in the current
 434 study. Since conducted preliminary RANS studies (not shown in
 435 this paper) indicate that especially the rotational effects extension
 436 lead to increased isentropic efficiencies, the observed performance
 437 improvement near the stall limit predicted by the DDES can be
 438 attributed to this modification.

439 **4.3 Details on local flow physics.** For further comparison
 440 with experimental measurements by Klausmann et al. [20], we ana-
 441 lyze the flow at the reference locations ME21 and ME30. Figure 7
 442 and Fig. 8 show the effect of turbulence modeling uncertainty on
 443 the total pressure and temperature ratios and draw the comparison
 444 with experimental data at ME30 downstream of the stator. The
 445 baseline simulation underpredicts the total pressure ratio for the
 446 design mass flow rate in Fig. 7 between 30% and 80% span, while
 447 an overprediction can be seen at the hub and tip. This overpre-
 448 diction of the total pressure ratio in the hub region is also present
 449 with decreasing mass flow rates from Fig. 7b to Fig. 7d. The
 450 baseline simulation rather coincides with the measurements at the
 451 mid-range mass flows, but tends to overpredict the total pressure
 452 ratio for $\dot{m}_{corr} = 14.78 \text{ kg/s}$. The contour plots in Fig. 8, show-

ing the total pressure ratio at ME30 with reference to the integral 453
 area-averaged value at ME15, reveals that none of the RANS simu- 454
 lations is able to reproduce the corner separation in the hub region, 455
 which is observed in the experiments. This is in accordance with 456
 the RANS studies by He et al. [21]. Recently Klausmann et al. [39] 457
 have shown experimentally that the stator hub cavity increases the 458
 hub corner separation and is a contributor to the total pressure 459
 losses. As the current CFD setup neglects this cavity completely, 460
 it is not expected to match the experiments in this region. This is 461
 also addressed in Section 4.6, where we highlight capabilities and 462

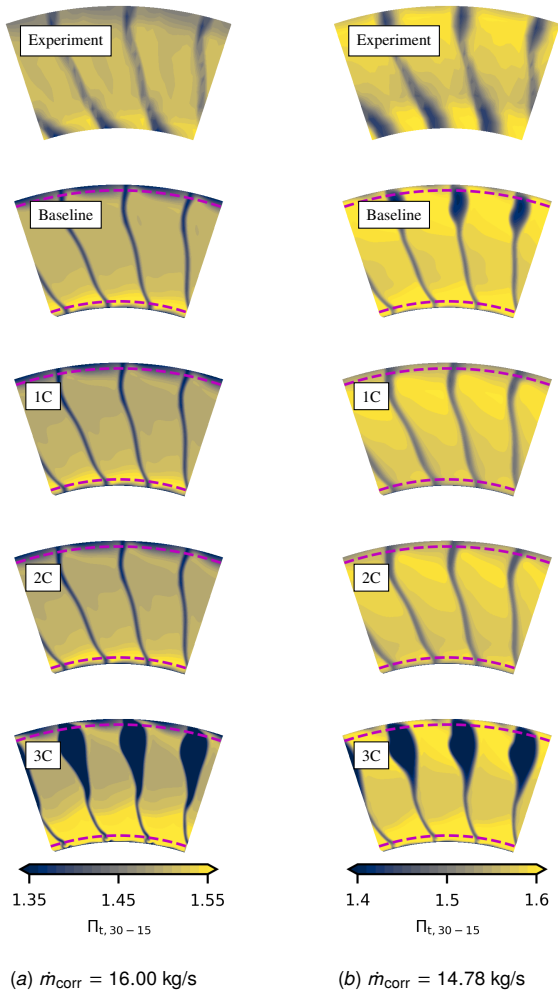


Fig. 8 Comparison of total pressure wake losses at ME30 for two different operating points. The total pressure and ratio is computed using the integral area-averaged total pressure at ME15. Red dashed lines indicate the radial measurement window in the experimental setup.

463 limitations of the applied UQ framework. Additionally, the wakes
 464 of the baseline, 1C and 2C simulation are predicted to be too sharp
 465 in comparison to the experiment, as can be observed in Fig. 8. It is
 466 important to acknowledge that the measured data are constrained
 467 by the spatial resolution inherent in the experiment. In general,
 468 1C and 2C perturbations tend to reduce the overpredicted pressure
 469 rise in all considered operating points but especially in the hub
 470 region for lower mass flow rates (see Fig. 7a to Fig. 7d), which
 471 indicates that the corner separation is characterised by anisotropic
 472 rather than isotropic Reynolds stresses. Perturbing the Reynolds
 473 stress tensor towards the isotropic state, massively affects the total
 474 pressure increase for higher mass flow rates. This means that the
 475 overprediction at the hub becomes larger, while the tip region
 476 is massively underpredicted, indicating near-tip trailing edge
 477 separation. This is supported by Fig. 13(b) presenting increased
 478 circumferentially area-averaged turbulent kinetic energy in the upper
 479 half of the annulus at ME30. Approaching the numerical stall
 480 limit, the over- and underprediction of experimental data by 3C
 481 simulation is reduced. Although the near hub regions seems to
 482 be sensitive to Reynolds stress tensor perturbation and, as was
 483 mentioned before, the 3C perturbation produces actual worst case
 484 total pressure, there is almost no coverage of the experimental and
 485 the DDES predicted total pressure ratios at ME30. Consequently,
 486 the turbulence model seems to be over-confident based on the to-

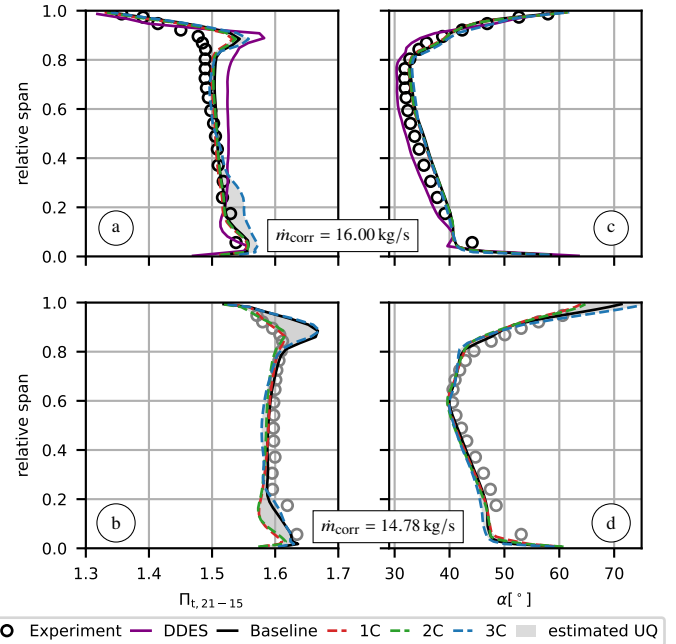


Fig. 9 Uncertainty estimates for predicting radial profiles of total pressure ratio ((a), (b)) and flow angle ((c), (d)) at ME21 for two different operating points. The total pressure ratio is computed using circumferentially area-averaged total pressure at ME21 and the integral area-averaged total pressure at ME15. Note: The experimental data presented in (b) and (d) were obtained by personal communication with Fabian Klausmann. As the underlying operation point ($\dot{m}_{\text{corr}} = 14.66 \text{ kg/s}$) varies slightly from the numerical one ($\dot{m}_{\text{corr}} = 14.78 \text{ kg/s}$), the markers are grayed out.

487 tal pressure prediction. Considering the total temperature ratio
 488 $\zeta_{t,30-15}$ at ME30 in Fig. 7e to Fig. 7h, the variation by means of
 489 tensor perturbations is small. Therefore, we can conclude that the
 490 effect of eigenvalue perturbation on the prediction of the total
 491 temperature is moderate. ME21 enables us to analyze the flow
 492 directly behind the rotor. Unfortunately, radial measurement data
 493 are not available for $\dot{m}_{\text{corr}} = 14.78 \text{ kg/s}$ at ME21, that is why
 494 Fig. 9b and Fig. 9d show experimental measurements at $\dot{m}_{\text{corr}} =$
 495 14.66 kg/s . Although the simulation results align well with the
 496 experimentally measured flow angle at the design speed in Fig. 9c,
 497 the total pressure ratio in Fig. 9a is overpredicted above 60%
 498 span by the RANS baseline simulation, due to the representation
 499 of the rotor tip vortex. Between 10% and 60% span the total
 500 pressure profiles are in accordance with the measurements. Nevertheless,
 501 the transitional DDES proves the existence of the total pressure
 502 increase due to the representation of the tip-leakage flow (see
 503 discussion on that by Möller et al. [33]). RANS also overpredicts
 504 the pressure increase in the very near hub region. Except for the
 505 tip and hub region at $\dot{m}_{\text{corr}} = 14.78 \text{ kg/s}$, perturbing the Reynolds
 506 stress tensor towards 1C and 2C lead to a minor decrease of total
 507 pressure ratio, while the flow angle is rather unaffected by this
 508 modification. Keeping in mind that the relative perturbation
 509 magnitude for 1C and 2C is significantly higher for the lower
 510 mass flow rate compared to the design point, we can conclude
 511 that the tip-leakage flow and the separation in the hub region
 512 (similarly to ME30) is prone to changes in the Reynolds stress
 513 tensor's anisotropy. The 3C perturbation leads to a pressure
 514 increase at the design mass flow rate in Fig. 9a. As opposed to
 515 this, the usage of $\Delta_B = 0.09$ at $\dot{m}_{\text{corr}} = 14.78 \text{ kg/s}$ results
 516 in almost unaffected total pressure ratio for 3C perturbation
 517 in Fig. 9c. Moreover, all considered eigenspace perturbations
 have moderate effect on the flow angle. This seems plausible as the

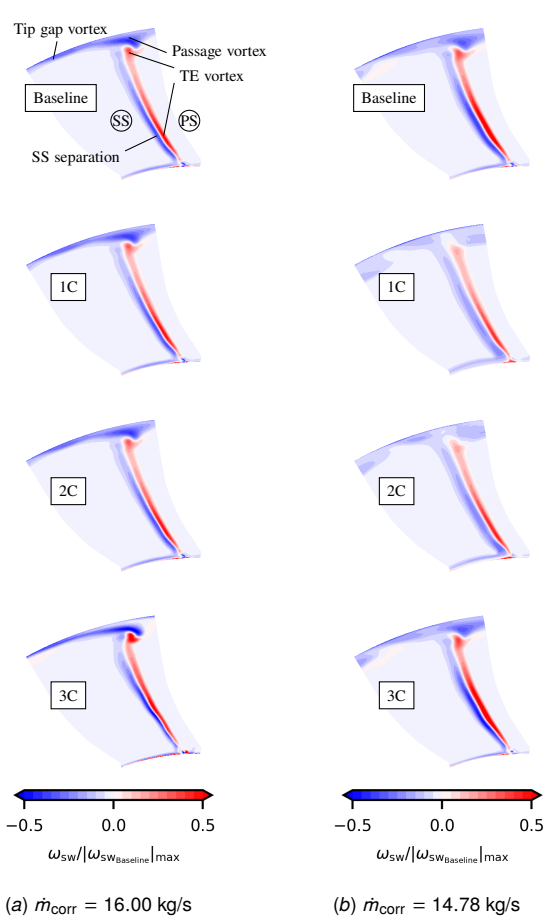


Fig. 10 Comparison of secondary flow structures indicated by the streamwise vorticity at Measurement plane (German: Messebene) (ME)21 for two different operating points. The local streamwise vorticity was normalized using the maximum absolute value of the streamwise vorticity occurring at ME21 in the baseline simulation.

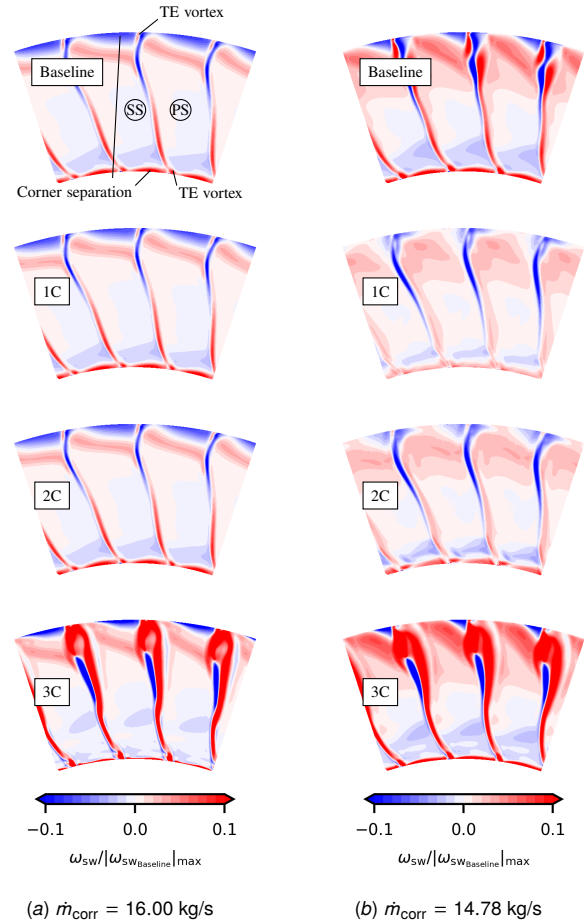


Fig. 11 Comparison of secondary flow structures indicated by the streamwise vorticity at ME30 for two different operating points. The local streamwise vorticity was normalized using the maximum absolute value of the streamwise vorticity occurring at ME30 in the baseline simulation.

518 turbulence modeling is not expected to have significant impact on
519 the flow turning.

520 The streamwise vorticity

$$521 \quad \omega_{sw} = \frac{U_i \epsilon_{ijk} \frac{\partial U_k}{\partial x_j}}{\sqrt{U_q U_q}} \quad (11)$$

522 enables an analysis of the secondary flow structures in the refer-
523 ence planes ME21 and ME30. The vortex system behind the rotor
524 is mainly dominated by a strong passage vortex on the suction side
525 (SS), which originates from the leading edge (LE) (see Fig. 10).
526 The flow at the tip gap of the rotor travels from pressure to SS,
527 merging with the passage vortex. The overpredicted total pressure
528 ratio at 90% span, as discussed above (see Fig. 9), can be attributed
529 to this secondary flow structure. Additionally, there are two vor-
530 tices coming from the pressure side (PS) near the trailing edge
531 (TE). The rotor's SS separation covers large parts of the entire span
532 (cf. Fig. 12(a)), causing increased streamwise vorticity in all con-
533 sidered simulations. On the one hand, the 1C and 2C simulations
534 only have limited effect on the vortex system at the design opera-
535 tion point. This is in accordance with the observations in Fig. 9,
536 keeping in mind that the perturbation magnitude is rather small.
537 On the other hand, 1C and 2C perturbations lead to mitigated sec-
538 ondary flows with the SS separation reduced in radial direction at
539 $\dot{m}_{corr} = 14.78 \text{ kg/s}$ (see Fig. 10(b) and Fig. 12(a)). In contrast to
540 the 1C and 2C perturbations, the perturbation towards the isotropic

limiting state does not alter the secondary flows at the near stall
operation point. However, 3C perturbation leads to the formation
of a separated vortex structure from the tip wall and increases the
vorticity formed by the TE vortices at $\dot{m}_{corr} = 16.00 \text{ kg/s}$.

Figure 11 presents the secondary flow at ME30. The flow behind
the stator reveals the existence of two corner separations at hub
and tip, which can be also identified in Fig. 12(b). Furthermore,
the flow past the TE causes the formation of vortices at hub and
tip. Throttling of the compressor leads to a massive increase of
streamwise vorticity (e.g. see baseline simulation in Fig. 11(b)).
Moreover, additional concentrated secondary flow structures occur,
if the simulation is close the achievable numerical stall limit (e.g.
baseline and 3C). These additional structures can be also identified
on the suction surface in Fig. 12(b). The eigenvalue perturbations
of the Reynolds stress tensor generally follow similar trends as
already described for ME21. To emphasize, one clearly sees that
3C perturbation underestimates the total pressure ratio in Fig. 7
and Fig. 8 above 40% span by producing massive vortex structures
at ME30.

4.4 Effect of anisotropy on turbulent kinetic energy level.

The reason for the observed behavior is the impact of the anisotropy
on the actual level of turbulence. The resulting distribution of
the turbulent kinetic energy is presented in Fig. 13 for three
operating points $\dot{m}_{corr} = 14.78 \text{ kg/s}$, $\dot{m}_{corr} = 15.12 \text{ kg/s}$ and
 $\dot{m}_{corr} = 15.84 \text{ kg/s}$. Following the theoretically derived relation-
ship between the production of turbulent kinetic energy and the

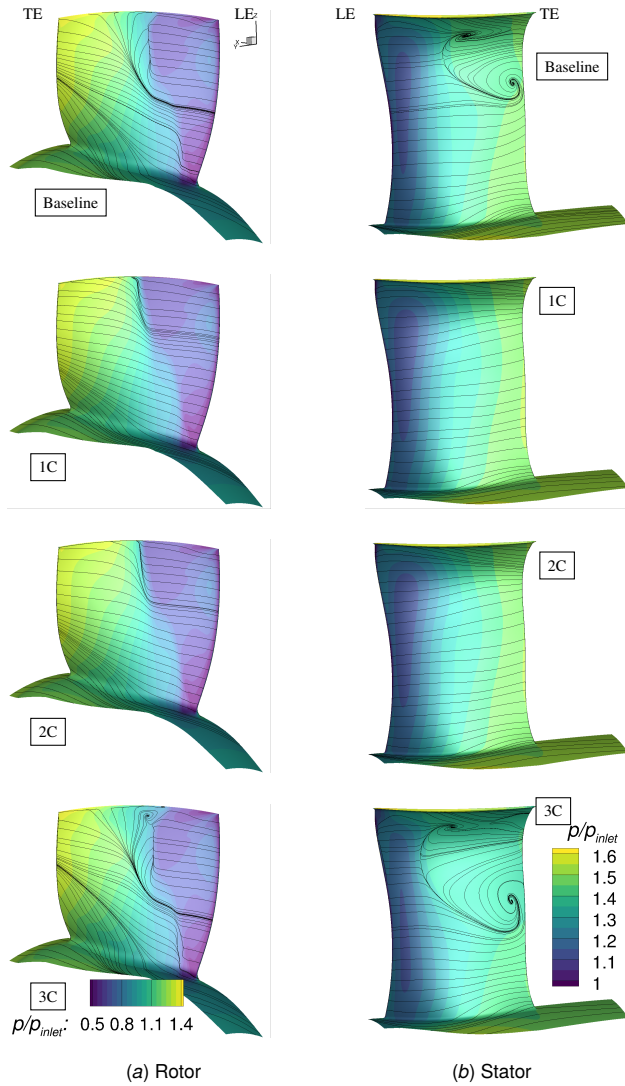
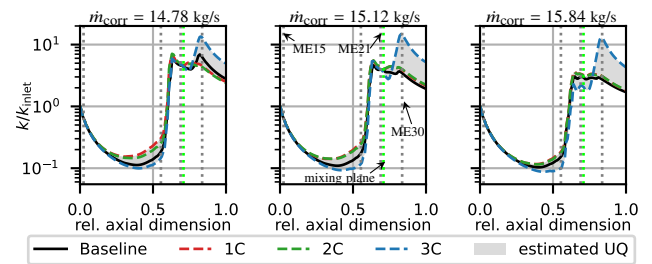


Fig. 12 The effect of perturbing the eigenspace of the Reynolds Stress tensor on static surface pressure and surface streamtraces on the hub and suction surfaces at $\dot{m}_{corr} = 14.78$ kg/s

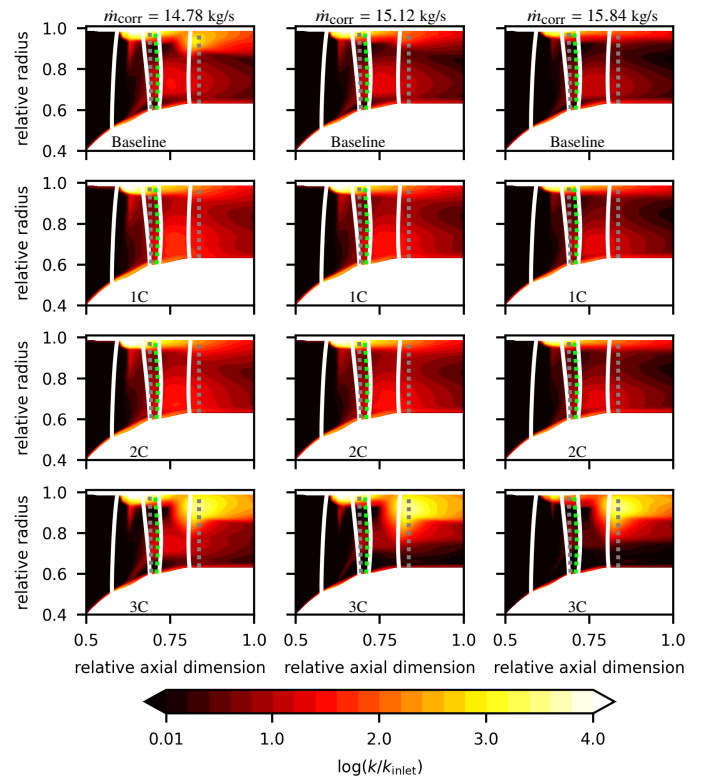
567 componentiality of turbulence [19,36], the turbulence production
 568 will be minimized by approaching the isotropic limit and maxi-
 569 mized for the 1C state². This can be observed in the upstream section
 570 before the rotor (relative axial dimension < 0.58) in Fig. 13(a),
 571 as the turbulence production is altered accordingly in the boundary
 572 layers at hub and tip. The circumferentially and radially area-
 573 averaged distribution of k is mostly unaffected by the eigenspace
 574 perturbation in the rotor section, as the increase of turbulence is
 575 mainly attributed to the superposition of occurring flow phenom-
 576 ena such as the formation of tip-leakage flow. The effect of a
 577 modified componentiality of the Reynolds stress tensor can be ob-
 578 served in the stator section again, where 3C turbulence creates large
 579 separation zones (cf. Fig. 12(b)) leading to increased turbulent ki-
 580 netic energy. Compared with the baseline simulation, the one- and
 581 two-component perturbation tends to decrease the turbulence level
 582 close to ME30 due to the suppression of separation zones at the
 583 near stall operation point (cf. Fig. 12(b)).

584 **4.5 Shock-boundary layer interaction.** Additionally, we ana-
 585 lyze the Mach number distributions across several constant ra-

²This is only valid if the velocity gradients are identical (cf. Eq. (7) and [19])



(a) Circumferentially and radially area-averaged turbulent kinetic energy over axial dimension of the compressor.



(b) Circumferential area-averaged 2D turbulent kinetic energy distribution in the core part of the compressor (zoom).

Fig. 13 Comparison of turbulent kinetic energy distribution throughout the compressor for three different operating points. Reference planes are shown by dotted gray lines, while the mixing plane interface between rotor and stator is marked in light green. White lines in (b) indicate the contours of rotor and stator.

586 dial planes. Figure 14, presenting the Mach number for $\dot{m}_{corr} =$ 586
 587 14.78 kg/s, confirms the previously described observations. Both 587
 588 the baseline and 3C simulation lead to massive separation in the 588
 589 stator tip region (relative span=0.9) (cf. Fig. 12(b)), while the one- 589
 590 and two-component perturbations result in sharper wakes with less 590
 591 losses. The region covering transient flow increases from hub to 591
 592 tip, which can be also seen in Fig. 12(a). The position of the 592
 593 shock in the passage of the rotor section is unaffected, whereas the 593
 594 shock's interaction with the boundary layer shows noticeable effects 594
 595 due to the eigenspace perturbation. Unfortunately, there is no 595
 596 measurement data available to judge the shock location predicted 596
 597 by RANS. That is the reason, why we included the numerical results 597
 598 based on the DDES at least for the design point in Fig. 15, 598

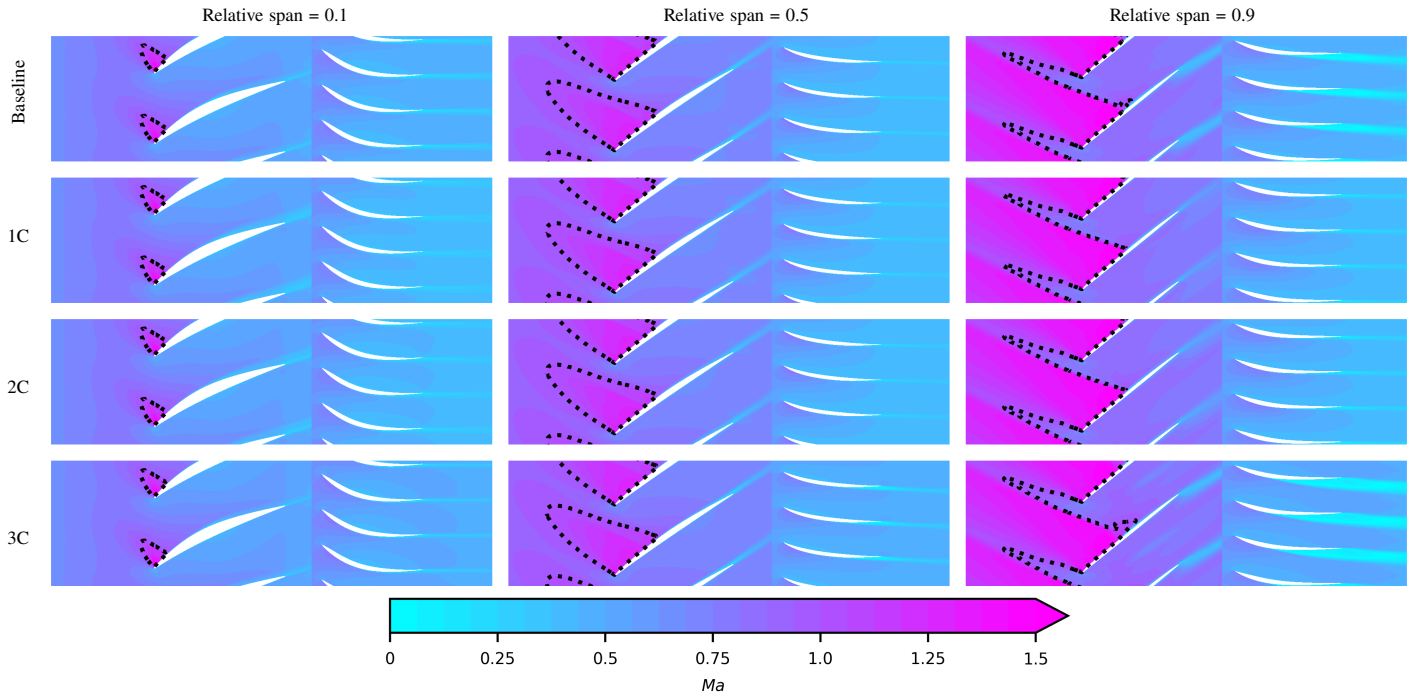


Fig. 14 Analysis of shock position and wake width prediction by illustrating the relative Mach number distribution for three constant relative span levels at $\dot{m}_{\text{corr}} = 14.78 \text{ kg/s}$.

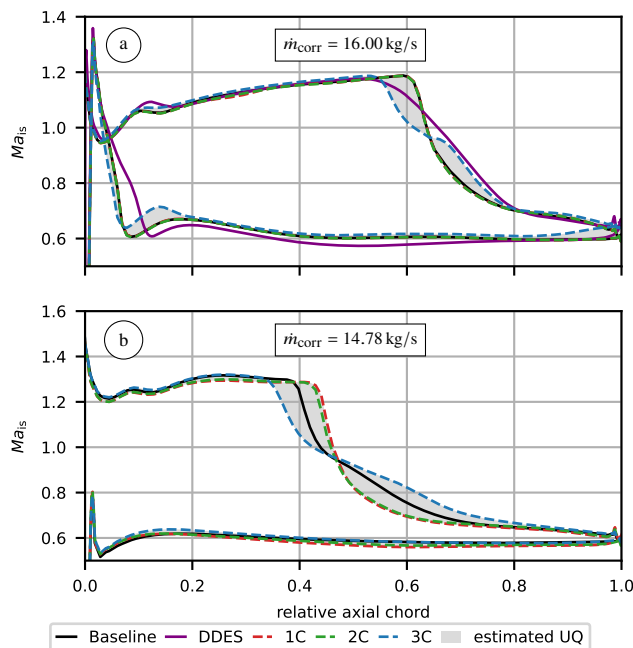


Fig. 15 Uncertainty estimates for the isentropic Mach number distribution at 90% span of the rotor for two different operating points.

location onset and steepness of the SS pressure increase. Nevertheless, the estimated uncertainty based on the EPF almost envelopes the DDES predicted drop in Ma_{is} . In accordance to the observations by Emory et al. [24], the isotropic perturbation lead to an earlier shock, the 1C and 2C perturbations postpone the shock-location. This becomes especially noticeable in off-design points (see Fig. 15b), when the relative perturbation magnitude increases for the 1C and 2C eigenvalue perturbations.

4.6 Capabilities and limitations of the EPF. The aim of the EPF is to quantify the epistemic uncertainties of LEVMs. Indeed, a turbomachinery designer is interested in attributing the effect of the turbulence model's uncertainty on certain design QoI. In the current work, this is achieved by perturbing the Reynolds stress tensor towards three limiting states of turbulence, propagating these states and observing the influence on QoIs. However, the relation between the 1C-, 2C- and 3C limiting state of the Reynolds stress tensor and some QoI is anything but linear. Consequently, the EPF seeks to estimate the uncertainty intervals rather than create extreme states for some QoI. Furthermore, we need to discuss the obvious judgment of the presented uncertainty intervals with respect to certain high-fidelity or measurement data, which is often done. There is no need that the simulation results, obtained by the EPF, overlap with reference data. The main reason is that the eigenvalue perturbation is only able to account for epistemic uncertainties limited to the turbulence model's representation of the turbulent state. Nevertheless, the LEVM's assumption that the Reynolds stress and strain-rate tensor have identical eigendirections (cf. Eq. (1)) is not necessarily valid. Thus, the incorporation of physically constrained eigenvector perturbations, as done in previous work [19], aiming to account for any misalignment with the eigenspace of the strain-rate tensor, is missing in the current analysis. Furthermore, other sources of uncertainties related to RANS simulations are not considered by the Reynolds stress tensor perturbations. In the current configuration of the TUDA-GLR-OpenStage compressor these might include the neglect of certain components (e.g. cavity), the inaccurate representation of the geometry (such as tip gap and fillet radii), the assumption of steady-state flow conditions, the application of the mixing plane approach at rotor-stator

599 showing the isentropic Mach number

$$600 \quad Ma_{\text{is}} = \sqrt{\left(\left(\frac{p_{t,21}}{p} \right)^{\frac{\gamma-1}{\gamma}} - 1 \right) \frac{2}{\gamma-1}} \quad (12)$$

601 at 90% of the rotor span. Comparing the baseline RANS with the
602 high-fidelity DDES simulation reveals some differences in shock-

641 interface, the use of 32 instead of 29 stator blades and, last but not
 642 least, the choice of the boundary conditions. Although we compare
 643 the RANS data with transitional DDES based on the research of
 644 Möller et al. [33] in order to mitigate geometrical uncertainties,
 645 there are still notable disparities in the simulation setups. These
 646 include variances in the approach to steady versus unsteady simulations,
 647 different numerical schemes and the application of multiple
 648 turbulence modeling modifications. Consequently, these simulations
 649 are not fully comparable. Therefore, it cannot be expected that
 650 the estimated uncertainties based on the EPF envelope the high-fidelity
 651 DDES. This is yet another illustration of the EPF's potential, as well as
 652 its limitations. Additionally, the achievable uncertainty intervals on
 653 QoIs such as the total pressure ratio or the overall isentropic efficiency
 654 of the compressor, are mainly affected by the prescribed amount of
 655 relative perturbation Δ_B . In the current study, we seek for worst
 656 case scenarios attributed to the maximum perturbation of the Reynolds
 657 stresses while still assuring convergence of the simulations. For this
 658 very reason, the presented uncertainties show the general trends of
 659 each individual eigenvalue perturbation. In a real world application,
 660 a designer would probably not try to use as much perturbation as
 661 possible across the entire speedline. Based on expert knowledge or
 662 machine learning strategies, a sensible strategy for future applications
 663 may be an application of non-uniform, more moderate eigenspace
 664 perturbations, both spatially in the computational domain and across
 665 multiple operating points.

667 5 Conclusion

668 We have presented the first multi-row turbomachinery application
 669 of the Reynolds stress tensor EPF to assess turbulence modeling
 670 uncertainty for the design speedline of the transonic TUDa-GLR-
 671 OpenStage compressor. Through comparison with measurement and
 672 transitional DDES data, we validate the ability of the EPF to quantify
 673 the epistemic uncertainties, showcasing its potential for complex
 674 turbomachinery simulations. In pursuit of worst case scenarios to
 675 ascertain the most conservative estimation of inherent turbulence
 676 modeling uncertainties, it is imperative to apply non-uniform
 677 relative perturbation magnitudes across the various operating
 678 points of the compressor and across different states of turbulence
 679 componentiality (1C, 2C, and 3C). The flow characteristics of the
 680 compressor allowed greater eigenvalue perturbation for 1C and 2C
 681 close to the numerical stall limit, whereas the perturbation
 682 towards the isotropic state could be increased near the design
 683 point.

684 Our current investigation underscores the sensitivity of determining
 685 the numerical stall limit of the compressor to the anisotropy of the
 686 Reynolds stress tensor, presenting a significant enhancement in
 687 accordance with the experimental stall limit compared to the
 688 baseline LEVM simulation. Consequently, orthotropic eddy viscosity
 689 models have the potential to provide stability improvements similar
 690 to conventional turbulence modeling enhancements. We postulate
 691 that this phenomenon can be attributed to the influence of
 692 turbulence componentiality on turbulence production. The evaluated
 693 radial profiles of total pressure also demonstrate that corner
 694 separations, and to some extent, the tip-leakage flow, are susceptible
 695 to changes in the shape of the Reynolds stress tensor ellipsoid.
 696 Although the baseline RANS model accurately captures the flow
 697 physics in the midsection, regions near the hub and tip consistently
 698 reveal deviations from measurements and pose challenges to
 699 designers. Therefore, the shown results based on the eigenvalue
 700 perturbation might be of great interest for turbomachinery
 701 designers and the turbulence modeling community. Finally, it was
 702 found that introducing substantial levels of anisotropy to the
 703 Reynolds stress tensor influences the dynamics of shock-boundary
 704 layer interaction, specifically affecting the location of the shock.
 705 The emphasized impacts of physically constrained perturbations
 706 on the shape of the Reynolds stress tensor offer new insights
 707 for future turbulence modeling approaches. The aim of these
 708 insights is to eliminate the need for non-physically constrained
 709 adjustments (often referred to

as *tweaking*) to the model in order to achieve a more accurate
 representation of compressor flow physics.

Last but not least, the current research paper, contributes to
 the evaluation of the epistemic turbulence modeling uncertainties
 for multi-row turbomachinery configurations, with a specific focus
 on the TUDa compressor. In future research, the inclusion of
 physically constrained eigenvector perturbations could complete
 the view of the true model-form uncertainty in the representation
 of the Reynolds stress tensor. As we have made the most
 conservative estimates, we believe that the next plausible step is
 to incorporate local perturbations in areas where LEVMs tend to
 fail while reducing the perturbation where the models are known
 to perform well.

Acknowledgments

This research is based on a project funded by MTU Aero Engines
 AG and the German Federal Ministry for Economic Affairs and
 Climate Action under the funding code 03EE5041A. Furthermore,
 we gratefully acknowledge Fabian Klausmann (Institute of Gas
 Turbines and Aerospace Propulsion at the Technical University
 of Darmstadt) for granting insights into the measurement
 campaign, providing the experimental data and always answering
 our questions.

References

- [1] Speziale, C. G. "Analytical Methods for the Development of Reynolds-Stress Closures in Turbulence." *Annual Review of Fluid Mechanics* Vol. 23 No. 1 (1991): pp. 107–157. doi: 10.1146/annurev.fl.23.010191.000543.
- [2] Mompean, G., Gavrilakis, S., Machiels, L. and Deville, M. "On predicting the turbulence-induced secondary flows using nonlinear $k-\epsilon$ models." *Physics of Fluids* Vol. 8 (1996): pp. 1856–1868. doi: 10.1063/1.868968.
- [3] Craft, T., Launder, B. and Suga, K. "Development and application of a cubic eddy-viscosity model of turbulence." *International Journal of Heat and Fluid Flow* Vol. 17 No. 2 (1996): pp. 108–115. doi: 10.1016/0142-727X(95)00079-6.
- [4] Lien, F. and Leschziner, M. "Assessment of turbulence-transport models including non-linear rng eddy-viscosity formulation and second-moment closure for flow over a backward-facing step." *Computers & Fluids* Vol. 23 No. 8 (1994): pp. 983–1004. doi: 10.1016/0045-7930(94)90001-9.
- [5] Oberkampf, W. and Roy, C. *Verification and Validation in Scientific Computing* (2010). doi: 10.1017/CBO9780511760396.
- [6] Karniadakis, G. "Quantifying Uncertainty in CFD." *Journal of Fluids Engineering-transactions of the ASME* Vol. 124 No. 1 (2002): pp. 2–3. doi: 10.1115/1.1447925.
- [7] Zang, T., Hemsch, M., Hilburger, M., Kenny, S., Luckring, J., Maghami, P., Padula, S. and Stroud, W. "Needs and Opportunities for Uncertainty-Based Multidisciplinary Design Methods for Aerospace Vehicles." (2002).
- [8] Duraisamy, K., Iaccarino, G. and Xiao, H. "Turbulence Modeling in the Age of Data." *Annual Review of Fluid Mechanics* Vol. 51 No. Volume 51, 2019 (2019): pp. 357–377. doi: <https://doi.org/10.1146/annurev-fluid-010518-040547>. URL <https://www.annualreviews.org/content/journals/10.1146/annurev-fluid-010518-040547>.
- [9] Xiao, H. and Cinnella, P. "Quantification of model uncertainty in RANS simulations: A review." *Progress in Aerospace Sciences* Vol. 108 (2019): pp. 1–31. doi: <https://doi.org/10.1016/j.paerosci.2018.10.001>. URL <https://www.sciencedirect.com/science/article/pii/S0376042118300952>.
- [10] Emory, M., Larsson, J. and Iaccarino, G. "Modeling of structural uncertainties in Reynolds-averaged Navier-Stokes closures." *Physics of Fluids* Vol. 25 No. 11 (2013): p. 110822. doi: 10.1063/1.4824659. URL https://pubs.aip.org/aip/pof/article-pdf/doi/10.1063/1.4824659/13379908/110822_1_online.pdf, URL <https://doi.org/10.1063/1.4824659>.
- [11] Mukhopadhyaya, J., Whitehead, B. T., Quindlen, J. F., Alonso, J. J. and Cary, A. W. "Multi-fidelity modeling of probabilistic aerodynamic databases for use in aerospace engineering." *International Journal for Uncertainty Quantification* Vol. 10 No. 5 (2020): pp. 425–447.
- [12] Lamberti, G. and Gorié, C. "Uncertainty Quantification for RANS Predictions of Wind Loads on Buildings." Ricciardelli, F. and Avossa, A. M. (eds.). *Proceedings of the XV Conference of the Italian Association for Wind Engineering*: pp. 402–412. 2019. Springer International Publishing, Cham.
- [13] Hornshøj-Møller, S. D., Nielsen, P. D., Foroughi, P. and Abkar, M. "Quantifying structural uncertainties in Reynolds-averaged Navier-Stokes simulations of wind turbine wakes." *Renewable Energy* Vol. 164 (2021): pp. 1550–1558. doi: <https://doi.org/10.1016/j.renene.2020.10.148>. URL <https://www.sciencedirect.com/science/article/pii/S0960148120317237>.
- [14] Eidi, A., Ghiassi, R., Yang, X. and Abkar, M. "Model-form uncertainty quantification in RANS simulations of wakes and power losses in wind farms." *Renewable Energy* Vol. 179 (2021): pp. 2212–2223. doi: <https://doi.org/10.1016/j.renene.2021.08.012>. URL <https://www.sciencedirect.com/science/article/pii/S0960148121011721>.

- 785 [15] Emory, M., Iaccarino, G. and Laskowski, G. M. "Uncertainty Quantification in Turbomachinery Simulations." Vol. Volume 2C: Turbomachinery: p. V02CT39A028. 2016. doi: 10.1115/GT2016-56798. URL <https://asmedigitalcollection.asme.org/GT/proceedings-pdf/GT2016/49712/V02CT39A028/2429368/v02ct39a028-gt2016-56798.pdf>, URL <https://doi.org/10.1115/GT2016-56798>.
- 786 [16] Geiser, G., Wellner, J., Kügeler, E., Weber, A. and Moors, A. "On the Simulation and Spectral Analysis of Unsteady Turbulence and Transition Effects in a Multistage Low Pressure Turbine." Vol. 141 No. 5 (2019). doi: 10.1115/1.4041820.
- 787 [17] Matha, M., Kucharczyk, K. and Morsbach, C. "Evaluation of physics constrained data-driven methods for turbulence model uncertainty quantification." *Computers & Fluids* Vol. 255 (2023): p. 105837. doi: <https://doi.org/10.1016/j.compfluid.2023.105837>. URL <https://www.sciencedirect.com/science/article/pii/S0045793023000622>.
- 788 [18] Matha, M. and Morsbach, C. "Improved self-consistency of the Reynolds stress tensor eigenspace perturbation for uncertainty quantification." *Physics of Fluids* Vol. 35 No. 6 (2023): p. 065130. doi: 10.1063/5.0149747. URL https://pubs.aip.org/aip/pof/article-pdf/doi/10.1063/5.0149747/18007124/065130_1_5.0149747.pdf, URL <https://doi.org/10.1063/5.0149747>.
- 789 [19] Matha, M. and Morsbach, C. "Physically constrained eigenspace perturbation for turbulence model uncertainty estimation." *Physics of Fluids* Vol. 36 No. 2 (2024): p. 025153. doi: 10.1063/5.0185841. URL https://pubs.aip.org/aip/pof/article-pdf/doi/10.1063/5.0185841/19692325/025153_1_5.0185841.pdf, URL <https://doi.org/10.1063/5.0185841>.
- 790 [20] Klausmann, F., Franke, D., Foret, J. and Schiffer, H.-P. "Transonic compressor Darmstadt - Open test case Introduction of the TUDA open test case." *Journal of the Global Power and Propulsion Society* Vol. 6 (2022): pp. 318–329. doi: 10.33737/jgpps/156120.
- 791 [21] He, X., Zhu, M., Xia, K., Fabian, K. S., Teng, J. and Vahdati, M. "Validation and verification of RANS solvers for TUDA-GLR-OpenStage transonic axial compressor." *Journal of the Global Power and Propulsion Society* Vol. 7 (2023): pp. 13–29. doi: 10.33737/jgpps/158034.
- 792 [22] Xia, K., He, X., Zhu, M., Klausmann, F. S., Teng, J. and Vahdati, M. "Endwall geometric uncertainty and error on the performance of TUDA-GLR-OpenStage transonic axial compressor." *Journal of the Global Power and Propulsion Society* Vol. 7 (2023): pp. 113–126. doi: 10.33737/jgpps/161708.
- 793 [23] He, X. and Klausmann, F. "RANS Capabilities for Transonic Axial Compressor: A Perspective from GPPS CFD Workshop." (2023).
- 794 [24] Emory, M., Pecnik, R. and Iaccarino, G. *Modeling Structural Uncertainties in Reynolds-Averaged Computations of Shock/Boundary Layer Interactions* (2011): doi: 10.2514/6.2011-479. URL <https://arc.aiaa.org/doi/pdf/10.2514/6.2011-479>, URL <https://arc.aiaa.org/doi/abs/10.2514/6.2011-479>.
- 795 [25] Iaccarino, G., Mishra, A. A. and Ghili, S. "Eigenspace perturbations for uncertainty estimation of single-point turbulence closures." *Phys. Rev. Fluids* Vol. 2 (2017): p. 024605. doi: 10.1103/PhysRevFluids.2.024605. URL <https://link.aps.org/doi/10.1103/PhysRevFluids.2.024605>.
- 796 [26] Mishra, A. A. and Iaccarino, G. "Theoretical analysis of tensor perturbations for uncertainty quantification of Reynolds averaged and subgrid scale closures." *Physics of Fluids* Vol. 31 No. 7 (2019): p. 075101. doi: 10.1063/1.5099176. URL https://pubs.aip.org/aip/pof/article-pdf/doi/10.1063/1.5099176/19770862/075101_1_online.pdf, URL <https://doi.org/10.1063/1.5099176>.
- 797 [27] Schumann, U. "Realizability of Reynolds-Stress Turbulence Models." *Physics of Fluids* Vol. 20 (1977): pp. 721–725. URL <https://api.semanticscholar.org/CorpusID:121481036>.
- 798 [28] Banerjee, S., Krahl, R., Durst, F. and Zenger, C. "Presentation of anisotropy properties of turbulence, invariants versus eigenvalue approaches." *Journal of Turbulence* Vol. 8 (2007): p. N32. doi: 10.1080/14685240701506896. URL <https://doi.org/10.1080/14685240701506896>, URL <https://doi.org/10.1080/14685240701506896>.
- 799 [29] Gorlé, C. and Iaccarino, G. "A framework for epistemic uncertainty quantification of turbulent scalar flux models for Reynolds-averaged Navier-Stokes simulations." *Physics of Fluids* Vol. 25 No. 5 (2013): p. 055105. doi: 10.1063/1.4807067. URL https://pubs.aip.org/aip/pof/article-pdf/doi/10.1063/1.4807067/15840261/055105_1_online.pdf, URL <https://doi.org/10.1063/1.4807067>.
- 800 [30] Heyse, J. F., Mishra, A. A. and Iaccarino, G. "Estimating RANS model uncertainty using machine learning." *Journal of the Global Power and Propulsion Society* No. May (2021): pp. 1–14. doi: 10.33737/jgpps/134643. URL <https://doi.org/10.33737/jgpps/134643>.
- 801 [31] Morsbach, C. "Reynolds Stress Modelling for Turbomachinery Flow Applications." Ph.D. Thesis, German Aerospace Center, Technische Universität Darmstadt, Darmstadt, Germany. 2017. URL <http://elib.dlr.de/113258/>.
- 802 [32] Menter, F., Kuntz, M. and Langtry, R. "Ten years of industrial experience with the SST turbulence model." *Turbulence, Heat and Mass Transfer* Vol. 4 (2003): pp. 625 – 632.
- 803 [33] Möller, F. M., Tucker, P. G., Wang, Z.-N., Bode, C., Morsbach, C., Matha, M. and Sivel, P. "Advanced Methods for Assessing Flow Physics of the TU Darmstadt Compressor Stage: Part I Transitional Delayed Detached-Eddy Simulation." Vol. Volume 12C: Turbomachinery Design Methods and CFD Modeling for Turbomachinery; Ducts, Noise, and Component Interactions: p. V12CT32A037. 2024. doi: 10.1115/GT2024-127679. URL <https://asmedigitalcollection.asme.org/GT/proceedings-pdf/GT2024/88070/V12CT32A037/7371296/v12ct32a037-gt2024-127679.pdf>, URL <https://doi.org/10.1115/GT2024-127679>.
- 804 [34] Schluß, D., Frey, C. and Ashcroft, G. "Consistent Non-Reflecting Boundary Conditions For Both Steady And Unsteady Flow Simulations In Turbomachinery Applications." *7th European Congress on Computational Methods in Applied Sciences And Engineering*. 2016.
- 805 [35] Emory, M. A. "Estimating model-form uncertainty in Reynolds-averaged Navier-Stokes closures." Ph.D. Thesis, Stanford University, Department of Mechanical Engineering. 2014.
- 806 [36] Gorlé, C., Zeoli, S., Emory, M., Larsson, J. and Iaccarino, G. "Epistemic uncertainty quantification for Reynolds-averaged Navier-Stokes modeling of separated flows over streamlined surfaces." *Physics of Fluids* Vol. 31 No. 3 (2019): p. 035101. doi: 10.1063/1.5086341. URL https://pubs.aip.org/aip/pof/article-pdf/doi/10.1063/1.5086341/15728751/035101_1_online.pdf, URL <https://doi.org/10.1063/1.5086341>.
- 807 [37] Kato, M. and Launder, B. "The Modelling of Turbulent Flow Around Stationary and Vibrating Square Cylinders." *9th Symposium on Turbulent Shear Flows*: pp. 10.4.1–10.4.6. 1993.
- 808 [38] Bardina, J., Ferziger, J. H. and Rogallo, R. S. "Effect of rotation on isotropic turbulence: computation and modelling." *Journal of Fluid Mechanics* Vol. 154 (1985): p. 321–336. doi: 10.1017/S0022112085001550.
- 809 [39] Klausmann, F., Kilian, N., He, X., Franke, D., Schmidt, B. and Schiffer, H.-P. "Transonic Compressor Darmstadt Open Test Case: Experimental Investigation of Stator Secondary Flows and Hub Leakage." *Turbo Expo: Power for Land, Sea, and Air*. Vol. Volume 13A: Turbomachinery — Axial Flow Fan and Compressor Aerodynamics: p. V13AT29A037. 2023. doi: 10.1115/GT2023-103502.
- 810
- 811
- 812
- 813
- 814
- 815
- 816
- 817
- 818
- 819
- 820
- 821
- 822
- 823
- 824
- 825
- 826
- 827
- 828
- 829
- 830
- 831
- 832
- 833
- 834
- 835
- 836
- 837
- 838
- 839
- 840
- 841
- 842
- 843
- 844
- 845
- 846
- 847
- 848
- 849
- 850
- 851
- 852
- 853
- 854
- 855
- 856
- 857
- 858
- 859
- 860
- 861
- 862
- 863
- 864
- 865
- 866
- 867
- 868
- 869
- 870
- 871

List of Figures

1	Systematic representation of the Reynolds stress tensor's eigenvalue perturbation within the barycentric triangle. Its effect on the shape of the Reynolds stress tensor is shown by the gray ellipsoid visualizations, when approaching the vertices of the triangle.	3
2	3D illustration of the considered TUDa compressor configuration. The simulated single passage is colored in pink, while reference locations are highlighted as well.	3
3	Effect of grid resolution on the prediction of total pressure ratio (top) and isentropic efficiency (bottom) by RANS at 100% speedline.	4
4	Attainable relative perturbation magnitude Δ_B over corrected mass flow rate for eigenvalue perturbation of the Reynolds stress tensor towards the three limiting states of turbulence.	5
5	Illustration of the turbulent state of the Reynolds stress tensor at ME30 and $\dot{m}_{\text{corr}} = 14.78 \text{ kg/s}$. (a) presents the RGB coloring according to the location of each data point inside the barycentric triangle, which is shown in (b).	5
	(a) RGB coloring	5
	(b) Barycentric coordinates	5
6	Estimated turbulence modeling uncertainty for the global compressor performance quantities total pressure ratio (top) and isentropic efficiency (bottom) at 100% speedline and comparison with experimental data. The mass flow rates for subsequent detailed analysis are highlighted by magenta dashed lines ($\dot{m}_{\text{corr}} \in [14.78 \text{ kg/s}, 15.12 \text{ kg/s}, 15.84 \text{ kg/s}, 16.00 \text{ kg/s}]$).	6
7	Uncertainty estimates for predicting radial profiles of total pressure ratio ((a), (b), (c), (d)) and total temperature ratio ((e), (f), (g), (h)) at ME30 for four different operating points. The total pressure and temperature ratio is computed using circumferentially area-averaged quantities at ME30 and the integral area-averaged quantities at ME15.	6
8	Comparison of total pressure wake losses at ME30 for two different operating points. The total pressure and ratio is computed using the integral area-averaged total pressure at ME15. Red dashed lines indicate the radial measurement window in the experimental setup.	7
	(a) $\dot{m}_{\text{corr}} = 16.00 \text{ kg/s}$	7
	(b) $\dot{m}_{\text{corr}} = 14.78 \text{ kg/s}$	7
9	Uncertainty estimates for predicting radial profiles of total pressure ratio ((a), (b)) and flow angle ((c), (d)) at ME21 for two different operating points. The total pressure ratio is computed using circumferentially area-averaged total pressure at ME21 and the integral area-averaged total pressure at ME15. Note: The experimental data presented in (b) and (d) were obtained by personal communication with Fabian Klausmann. As the underlying operation point ($\dot{m}_{\text{corr}} = 14.66 \text{ kg/s}$) varies slightly from the numerical one ($\dot{m}_{\text{corr}} = 14.78 \text{ kg/s}$), the markers are grayed out.	7
10	Comparison of secondary flow structures indicated by the streamwise vorticity at ME21 for two different operating points. The local streamwise vorticity was normalized using the maximum absolute value of the streamwise vorticity occurring at ME21 in the baseline simulation.	8
	(a) $\dot{m}_{\text{corr}} = 16.00 \text{ kg/s}$	8
	(b) $\dot{m}_{\text{corr}} = 14.78 \text{ kg/s}$	8
11	Comparison of secondary flow structures indicated by the streamwise vorticity at ME30 for two different operating points. The local streamwise vorticity was normalized using the maximum absolute value of the streamwise vorticity occurring at ME30 in the baseline simulation.	8
	(a) $\dot{m}_{\text{corr}} = 16.00 \text{ kg/s}$	8
	(b) $\dot{m}_{\text{corr}} = 14.78 \text{ kg/s}$	8
12	The effect of perturbing the eigenspace of the Reynolds Stress tensor on static surface pressure and surface streamtraces on the hub and suction surfaces at $\dot{m}_{\text{corr}} = 14.78 \text{ kg/s}$	9
	(a) Rotor	9
	(b) Stator	9
13	Comparison of turbulent kinetic energy distribution throughout the compressor for three different operating points. Reference planes are shown by dotted gray lines, while the mixing plane interface between rotor and stator is marked in light green. White lines in (b) indicate the contours of rotor and stator.	9
	(a) Circumferentially and radially area-averaged turbulent kinetic energy over axial dimension of the compressor.	9
	(b) Circumferential area-averaged 2D turbulent kinetic energy distribution in the core part of the compressor (zoom).	9
14	Analysis of shock position and wake width prediction by illustrating the relative Mach number distribution for three constant relative span levels at $\dot{m}_{\text{corr}} = 14.78 \text{ kg/s}$	10
15	Uncertainty estimates for the isentropic Mach number distribution at 90% span of the rotor for two different operating points.	10

List of Tables

1	Number of grid points / 10^6 used for the RANS grid convergence study presented in Fig. 3.	4
---	--	---